

RESEARCH

Open Access



The multiple *de novo* copy number variant (*MdnCNV*) phenomenon presents with peri-zygotic DNA mutational signatures and multilocus pathogenic variation

Haowei Du^{1†}, Angad Jolly^{1,2†}, Christopher M. Grochowski^{1†}, Bo Yuan^{1,3,4,5}, Moez Dawood^{1,2,5}, Shalini N. Jhangiani⁵, He Li⁵, Donna Muzny⁵, Jawid M. Fatih¹, Zeynep Coban-Akdemir^{1,6}, Mary Esther Carlin^{7^}, Angela E. Scheuerle^{7,8,9}, Karin Witzl^{10,11}, Jennifer E. Posey¹, Matthew Pendleton¹², Eoghan Harrington¹², Sissel Juul¹², P. J. Hastings^{1,13}, Weimin Bi^{1,3}, Richard A. Gibbs^{1,5}, Fritz J. Sedlazeck^{1,5}, James R. Lupski^{1,5,14,15*}, Claudia M. B. Carvalho^{1,16*} and Pengfei Liu^{1,3*} 

Abstract

Background: The multiple *de novo* copy number variant (*MdnCNV*) phenotype is described by having four or more constitutional *de novo* CNVs (*dnCNVs*) arising independently throughout the human genome within one generation. It is a rare peri-zygotic mutational event, previously reported to be seen once in every 12,000 individuals referred for genome-wide chromosomal microarray analysis due to congenital abnormalities. These rare families provide a unique opportunity to understand the genetic factors of peri-zygotic genome instability and the impact of *dnCNV* on human diseases.

Methods: Chromosomal microarray analysis (CMA), array-based comparative genomic hybridization, short- and long-read genome sequencing (GS) were performed on the newly identified *MdnCNV* family to identify *de novo* mutations including *dnCNVs*, *de novo* single-nucleotide variants (*dnSNVs*), and indels. Short-read GS was performed on four previously published *MdnCNV* families for *dnSNV* analysis. Trio-based rare variant analysis was performed on the newly identified individual and four previously published *MdnCNV* families to identify potential genetic etiologies contributing to the peri-zygotic genomic instability. Lin semantic similarity scores informed quantitative human phenotype ontology analysis on three *MdnCNV* families to identify gene(s) driving or contributing to the clinical phenotype.

Results: In the newly identified *MdnCNV* case, we revealed eight *de novo* tandem duplications, each ~1 Mb, with microhomology at 6/8 breakpoint junctions. Enrichment of *de novo* single-nucleotide variants (SNV; 6/79) and *de*

[†]Haowei Du, Angad Jolly, and Christopher M. Grochowski contributed equally to this study.

[^]Mary Esther Carlin is deceased.

*Correspondence: jlupski@bcm.edu; ccarvalho@pnri.org; pengfeiliu@bcm.edu

¹ Department of Molecular and Human Genetics, Baylor College of Medicine, One Baylor Plaza, Houston, TX 77030, USA

¹⁶ Pacific Northwest Research Institute, 720 Broadway, Seattle, WA 98122, USA

Full list of author information is available at the end of the article



novo indels (1/12) was found within 4 Mb of the *dn*CNV genomic regions. An elevated post-zygotic SNV mutation rate was observed in *Mdn*CNV families. Maternal rare variant analyses identified three genes in distinct families that may contribute to the *Mdn*CNV phenomenon. Phenotype analysis suggests that gene(s) within *dn*CNV regions contribute to the observed proband phenotype in 3/3 cases. CNVs in two cases, a contiguous gene duplication encompassing *PMP22* and *RAI1* and another duplication affecting *NSD1* and *SMARCC2*, contribute to the clinically observed phenotypic manifestations.

Conclusions: Characteristic features of *dn*CNVs reported here are consistent with a microhomology-mediated break-induced replication (MMBIR)-driven mechanism during the peri-zygotic period. Maternal genetic variants in DNA repair genes potentially contribute to peri-zygotic genomic instability. Variable phenotypic features were observed across a cohort of three *Mdn*CNV probands, and computational quantitative phenotyping revealed that two out of three had evidence for the contribution of more than one genetic locus to the proband's phenotype supporting the hypothesis of *de novo* multilocus pathogenic variation (MPV) in those families.

Keywords: Long-read sequencing, Genomic data integration, Genomic data visualization, MMBIR, Genomic instability, Tandem duplication, *De novo* CNV, *De novo* SNV, Human Phenotype Ontology, Structural variation

Background

De novo copy number variants (*dn*CNVs) that occur during gametogenesis or early post-zygotic development are present in all or most cells of a multicellular organism. Genome-wide surveys of large populations estimate the *de novo* mutation rate for structural variants to be 0.16–0.29 events per generation in humans [1, 2]. The rate for *dn*CNVs with a length over 100 kb is lower, around 0.012 per haploid genome [3]. A unique mutational phenomenon described by Liu et al. highlighted individuals with variable congenital abnormalities and multiple ($n \geq 4$) *dn*CNVs (*Mdn*CNV) throughout their genome [4]. The *Mdn*CNV event, or phenomenon, can encompass several genes at each CNV locus [4].

*Mdn*CNV is a rare mutational phenomenon, identified in only 5/60,000 individuals referred for genome-wide chromosomal microarray analysis [4]. *Mdn*CNV has likely been under-appreciated due to the limited genomic resolution in clinical testing. The prominent features of *dn*CNVs shared between *Mdn*CNV cases include (1) a predominance of copy number gains across multiple chromosomes, (2) tandem duplications forming the majority of copy number gains, (3) the presence of sequence microhomology or microhomeology at breakpoint junctions, and (4) other mutational signatures of SV mutagenesis such as the DUP-TRP-DUP pattern of Complex Genomic Rearrangement (CGR) [4].

The variable congenital abnormalities observed in individuals exhibiting the *Mdn*CNV phenomenon are thought to be caused by the copy number change of different critical driver gene(s) in each proband. The Human Phenotype Ontology (HPO) represents a structured language database of human phenotype terms that allows for numerical coding of clinical phenotypes as HPO terms; such phenotypes may be observed in a proband or described in association with a gene or rare

disease trait clinical synopsis in OMIM [5]. This numerical coding enables quantitative, computational analyses of a patient's phenotypic features and comparison with phenotype associations within the literature to inform genomic variant prioritization.

Here we report a new family with multiple *dn*CNVs and leverage multiple genomic and phenotypic methodologies combined with visualization tools to extend our understanding of the *Mdn*CNV mutational phenomenon. Rare variant and mutational signature analyses on the newly described and four previously characterized *Mdn*CNV families suggest a maternal genetic variant contributing to peri-zygotic genome instability. Gene content of the affected genomic regions was analyzed using HPO to identify potential driver gene(s) and explore the hypothesis that the observed trait manifestation may be driven by multilocus pathogenic variation (MPV).

Methods

Subjects

The newly identified *Mdn*CNV family (HOU3579) was initially ascertained through clinical chromosomal microarray analysis (CMA) performed at Baylor Genetics. Written consents were obtained for the proband (BAB9637), unaffected siblings (BAB9640, BAB9641, and BAB9642), and parents (BAB9638 and BAB9639) to perform further genomic studies. Oligo array-based comparative genomic hybridization (aCGH) was performed on all family members ("Methods" section). Illumina short-read (SR) whole-genome sequencing (WGS) and long-read (LR) WGS with Oxford Nanopore Technologies (ONT) were performed on the proband and parents' blood leukocyte-derived DNA (Additional file 1: Supplementary methods). PacBio LR genomic sequencing was performed on the proband alone ("Methods"). Illumina

short-read WGS was performed on nine anonymized families under a separate IRB protocol with a waiver of consent, including four previously reported *MdnCNV* families (BAB3097, BAB3596, mCNV3/BAB9484, and mCNV7) [4] and five additional families without a *MdnCNV* phenotype as controls (Additional file 1: Supplementary methods).

Array comparative genomic hybridization

The family's DNA samples were initially analyzed by a clinical chromosomal microarray analysis (CMA) designed and performed by Baylor Genetics (BG) [6, 7]. Subsequently, high-resolution aCGH, using a 1 million probe whole-genome oligonucleotide microarray (Agilent microarray design ID:085903), was performed on all family members. All array-based experiments were implemented according to the Agilent aCGH protocol for probe labeling and hybridization with minor modifications [8].

Illumina SR sequencing

Genome sequencing was performed on proband and parents with an average read depth of $35\times$ at the Baylor College of Medicine Human Genome Sequencing Center. Please refer to supplementary material for the details.

Pacific Biosciences (PacBio) LR sequencing data

PacBio LR genomic sequencing was performed on the proband alone. The sequencing library was constructed with 5 μg genomic DNA using the SMRTbell Express Template Preparation Kit with an average insert size of 7.5 kb. The library was sequenced with five SMRTcells using the PacBio Sequel I instrument, which yielded 42 Gb of data.

Nanopore trio LR sequencing and mapping

LR sequencing libraries were generated according to standard Oxford Nanopore Technologies (ONT) protocols. Detailed sequencing process and metrics are provided (Additional file 1: Supplementary methods and Table S1). Average coverage of $25\times$ was achieved for the trio.

De novo single-nucleotide variant (SNV) and indel variant calling

Individual germline SNVs and indels were called using GATK (v.4.1.3) haplotypcaller and the HGSC xAtlas variant calling pipelines [9]. The “-GVCF” option was used for the GATK haplotypcaller, which outputs a gVCF file that includes reference or variant sequence information for all nucleotide positions. Using recalibrated posterior genotype probabilities to allow rigorous calling, *de novo* variants ($\text{GQ} \geq 20$ for all trio members) were annotated.

All possible *de novo* variants were further annotated using DNM (*de novo* mutation)-Finder (<https://github.com/BCM-Lupskilab/DNM-Finder>) [10], and manual inspection with Integrative Genomics Viewer (IGV) software was applied to confirm or reject the variant. It was performed with the following criteria per variant: (1) supported by at least 5 uniquely mapped reads; (2) supported by both forward and reverse strand reads; (3) variant did not derive from misalignment at indel variants; (4) not located at highly repetitive regions masked by RepeatMasker file for reference genome GRCh38 extracted from UCSC browser. In addition, potential *de novo* SNVs mapping within 20 bp of each other (clustered SNVs) was error-prone and thus removed from this study. *De novo* substitutions with variant read to total read ratio less than 0.35 or more than 0.65 ($\text{VR/TR} < 0.35$ or $\text{VR/TR} > 0.65$ and no read detected in any parental samples to exclude potential mosaicism in the parental genome) were classified as possible post-zygotic variant allele events.

Mutational pattern analysis

The R/Bioconductor package MutationalPatterns [11] was used for mutational signatures analysis on *dn*SNVs. The “cos_sim_matrix” function within the MutationPatterns package was used to calculate the cosine similarity between known COSMIC (v3.2) signatures [12] with the base substitution profile of *MdnCNV* families (Additional file 2: Table S2). To avoid overfitting, an unbiased refitting procedure was used to select the optimal combination of signatures using “fit_to_signatures_strict” function with “best_subset” method option. In short, the refitting process starts with a subset of signatures and then removes the signature that has the least contribution. The removal happens iteratively until it gets to the optimal subset.

Phasing SNVs and CNVs with combined read-based and pedigree-based method

The read-based phasing was performed using the publicly available WhatsHap tool [13]. In-house developed R scripts (<https://github.com/BCM-Lupskilab/PhaseDenovo>) were used to perform pedigree-based genetic phasing of physical haplotype blocks. The script assigns parental origin to the physical haplotype block if there are ≥ 20 informative SNPs present, and $\geq 90\%$ of them are consistent with a single parental origin. The *dn*SNVs were assigned to the parental chromosome based on segregated haplotype blocks. The *dn*CNVs were phased using the method as previously described [14].

Structural variant (SV) calling and analyses

Binary sequence alignment (BAM) files from SR and LR sequencing were used for SV calling. For Illumina SR, SVs were called and genotyped using Parliament2 [15]. Sniffles [16] was used for LR SV calling on the proband using the following parameters to maximize sensitivity: “-s 8”. The SV calls from the proband were genotyped based on parental BAM files using Sniffles with the option “-Ivcf”. Subsequently, SVs called exclusively in the proband were filtered with SURVIVOR allowing a maximum distance of 1000 bp between pairwise breakpoint junction calls from each algorithm. For *dnCNVs*, the log₂ ratio of read depth was visualized and manually examined (See “Visualization of genomics data for *dnCNVs*”) to minimize false-positive calls.

Breakpoint junction amplification and sequencing analysis

Soft-clipped reads overlapping breakpoint junctions were extracted from LR sequence alignment files and remapped to the human genome (GRCh38) with the UCSC BLAT tool to single base-pair resolution. The amplified breakpoint junctions were confirmed by Sanger dideoxynucleotide sequencing. The presence of non-B DNA-forming sequence motifs, including Z-DNA, G-quadruplex, A-phased repeats, inverted repeats, mirror repeats, and direct repeats, were screened for within 50 bp to either side of the breakpoint junctions using the reference genome and the nBMST tool [17].

De novo mutation rate estimation and statistical analysis for SNV clustering

The unphased genome-wide mutation rate per base-pair was estimated by taking the total number of DNMs divided by the size of the mappable diploid human reference genome (GRCh38). The phased genome-wide mutation rate was estimated by taking the total number of phased DNMs divided by the size of the mappable haploid human reference genome. The mappable human genome size (2.91 Tb/haploid genome) was computed using faCount from Kent's tool (http://hgdownload.soe.ucsc.edu/admin/exe/linux.x86_64/). The number of phased DNMs to each haploid type was extrapolated based on the ratio of successfully phased DNMs. The interval defined was centered on the ~1 Mb *dnCNV* with an additional 4 Mb window size flanking either side, representing ~9 Mb intervals in total for an individual *dnCNV*. The dynamic window size ranged from 1 to 10 Mb. The observed count of DNMs in eight *dnCNV* regional intervals was calculated in reference to the size of the window range used. The corresponding Poisson probability was calculated by multiplying the genome-wide DNM density by the corresponding *dnCNV* interval length. The average count of DNMs at the same genomic intervals

from 2976 genome sequenced trios [18] was calculated as the regional density control. The Poisson probability of observing the same or more DNMs was calculated using the ppois function from the R base package to determine the *p*-value.

Visualization of genomics data for *dnCNVs*

The average read depth from SR sequencing was calculated using mosdepth v0.2.3 with the “- by 1000” option. We used the median read depth of each chromosome to normalize the read depth of that chromosome and calculated the log₂ ratio for each 1000-bp window. The log₂ ratio profiles were segmented using the Circular Binary Segmentation (CBS) algorithm [19] implemented in the DNACopy Bioconductor package. The individual and segmented ratios were visualized together across genomic coordinates using Karyoploter (v.1.16.0) [20] with log₂ ratios of 0 representing normal copy number state, >0.58 representing copy number gains, and <-1 representing copy number loss.

Quantitative phenotyping analyses

To perform quantitative phenotype analysis, we used a similar method to that previously published [21–23] with modification; a detailed description follows. The patient's clinical description was translated to HPO terms using Doc2Hpo [24] and manually verified. HPO encoded phenotypes are available for known disease genes through Online Mendelian Inheritance in Man (OMIM.org) [25]. HPO encoded phenotypes for known diseases were extracted from OMIM and Orphanet. Using the ontologyX suite of R packages [26], a pairwise Lin semantic similarity score [27] was calculated between the patient's HPO term set and the HPO term sets of all known genes encompassed by proband *dnCNVs*. To assess for multilocus pathogenic variation, the phenotypic similarity score of the proband was compared to the combined phenotype associated with sets of known disease-associated genes encompassed by *dnCNVs*. Due to the limited sample size, a cutoff of 5% was arbitrarily selected to aid in the determination of multilocus pathogenic variation in conjunction with phenotypic overlap assessed by grid comparison of proband and disease gene-associated phenotypes.

Results

Ascertainment and identification of a new individual with genomic *MdnCNV* phenotype

Since the identification of the five *MdnCNV* families at Baylor Genetics (BG) [4], another individual (BAB9637) with potential *MdnCNV* was identified at BG. Clinical CMA performed on proband DNA revealed seven large, ~1 Mb, rare variant copy number gains mapping

to seven different chromosomes. In addition, an apparent 7 Mb absence of heterozygosity (AOH) genomic region was observed in exome sequencing data mapping to chromosome 15q14q21.1. To capture the full spectrum of *dnCNVs*, the subject, siblings, and parents' DNA was analyzed further in the research setting using a high-resolution aCGH. Short- and long-read genome sequencing was performed on proband and parental DNA with an average depth of coverage of $35\times$ and $25\times$, respectively. This multimodal genomic analysis approach (Fig. 1a, b, Additional file 1: Table S3) demonstrated eight tandem duplications, confirming the seven duplications previously identified on clinical CMA and revealing an eighth duplication not previously detected. The eight duplications mapped to different chromosomes and showed their sizes ranged from 899.1 to 1041.6 kb, i.e., ~ 1 Mb.

The high-resolution aCGH and breakpoint PCR confirmed that these eight duplications were only present in the proband (Fig. 1c and Additional file 1: Figures S1, S2). However, the apparent 7 Mb AOH region observed in chr15q14q21.1 by clinical CMA was not supported by the B-allele frequency calculated from genome sequencing data. This is likely due to genome sequencing interrogating a higher density of SNP sites ($n=9080$) compared to clinical CMA ($n=50$) (Additional file 1: Figure S3). An apparently homozygous ~ 60.2 kb deletion was identified within a rare *de novo* duplication on chromosome 14. Both parents are heterozygous for the deletion. The allele frequency of the deletion in the control population is 0.139 based on an allele count of 2990/21518 alleles in the gnomAD SV v2.1 database. The deletion allele frequency ranges from 0.043 in the African population to 0.339 in the Latino population (Additional file 1: Figure S4). We explored the potential association between both replication time and CNV regions by overlapping the duplication region to the replication time map of four embryonic stem cell lines [28]. Our analysis did not suggest a preference of *dnCNV* occurring regarding replication timing, i.e., *dnCNVs* were mapped to either late or early replication regions. Only microhomologies were found at the breakpoint junction for five *dnCNVs* (Additional file 1: Figure S1) which suggests a replicative instead of homologous recombination-based mechanism for the *dnCNV* formation in this case.

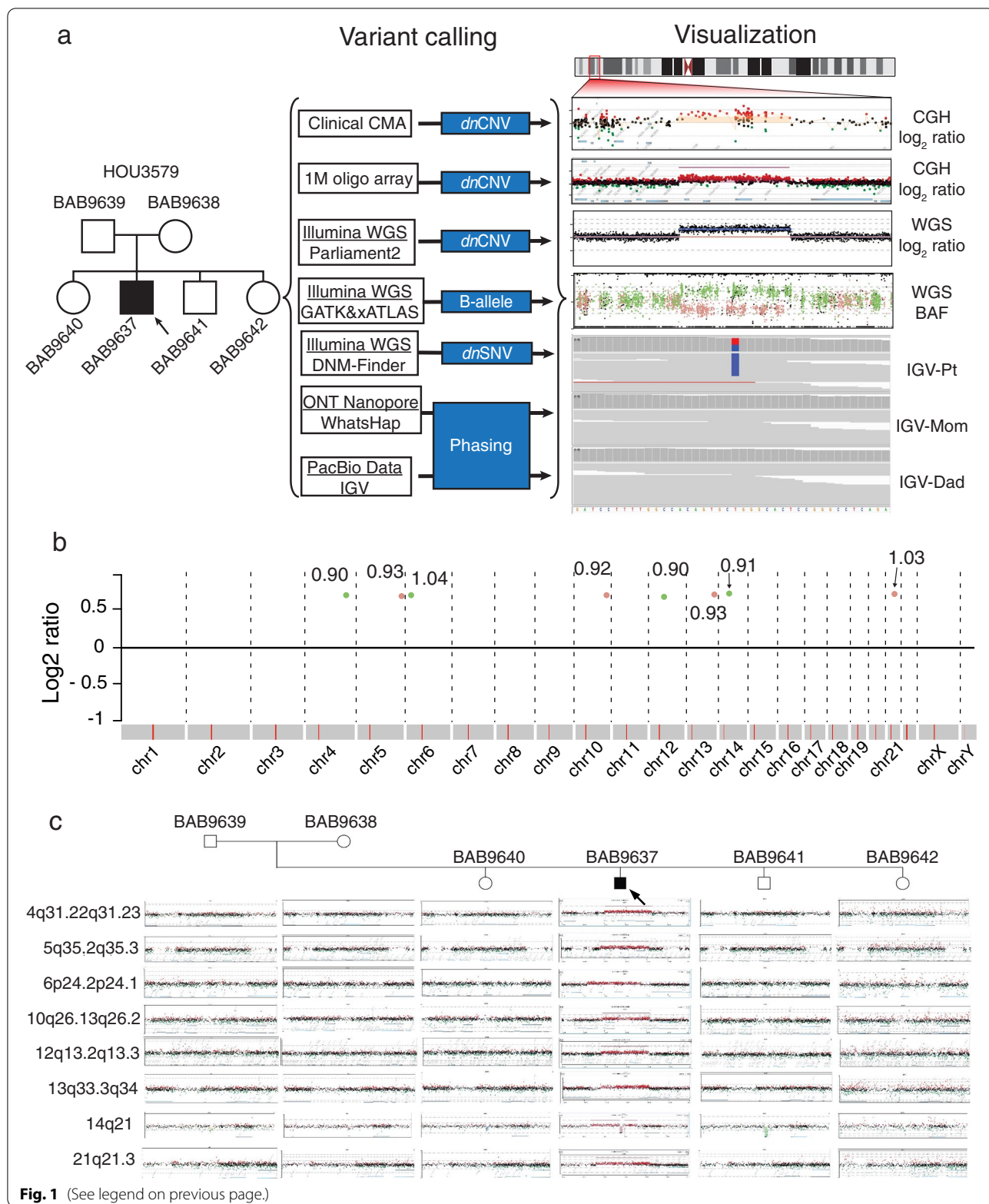
With SR sequencing data, we identified 91 DNMs including 79 SNVs (transition to transversion ratio [Ti:Tv]=2.0) and 12 indels (Fig. 2 and Additional file 3: Table S4). By combining short- and long-read sequencing data, we were able to phase 50 *dnSNVs*, of which 80% were of paternal origin (Additional file 3: Table S4). The predominance of paternal inheritance of *dnSNVs* was anticipated due to the accumulation of variants in aging male gametes [29, 30]. The genomic mapping of *dnSNVs* on the haploid human genome reference did not show any obvious clustering of variants. We calculated the distance of DNM to the nearest *dnCNV* breakpoint and found 7 (8.2%) DNMs within 4 Mb of the nearest breakpoint (Additional file 3: Table S4 and Fig. 2). The density of DNMs within 4 Mb of the breakpoint junctions was significantly higher than expected based on the number of DNMs and size of the genome (Additional file 1: Table S5, Fig. 2d) and was also significantly higher than the density of DNMs at the same genomic location in approximately 3000 control genomes [18]. We considered only the phased DNMs *in cis* with *dnCNVs*, which revealed that the observed density of DNMs was significantly higher than expected for either the maternal or paternal inherited haploid genome consistent with the hypermutation hypothesis [14, 31] of an underlying error-prone repair mechanism, microhomology-mediated break-induced replication (MMBIR) producing both CNVs and local SNVs (Additional file 1: Table S5).

Elevated post-zygotic *de novo* substitution rate in *MdnCNV* families

In addition to the new *MdnCNV* family (BAB9637), four previously reported *MdnCNV* families (BAB3097, BAB3596, mCNV3/BAB9484, and mCNV7, Table 1) were genome sequenced with an average depth of coverage of $40\times$. Through clinical array analysis, five anonymized families ascertained without *MdnCNV* were included as controls. We identified 470 (transition to transversion ratio [Ti:Tv]=2.2, 95% confidence interval (CI)=1.62–2.30) and 361 ([Ti:Tv]=2.2, CI=1.29–3.1) high-confidence *de novo* substitutions in *MdnCNV* and control families, respectively. SNV substitution mutations that occur during early development can lead to mosaicism in peripheral blood

(See figure on next page.)

Fig. 1 *dnCNV* and *dnSNV* identified with multiple genomic approaches. **a** Pedigree (left) of the *MdnCNV* family HOU3579. In the middle, the sequencing platform and variant calling pipeline are illustrated. Shown on the right, from top to bottom, is the visualization of an example of *dnCNV* in CMA, 1 M aCGH, short-read genome sequencing read depth, short-read genome sequencing B-allele frequency, and IGV view a high-quality *dnSNV* call. **b** Log₂ ratio of phased *dnCNV* in genome-wide view with chromosomes along the x-axis. Gains present on chromosomes 4, 6, 12, and 14 are each indicated with a green dot representing duplication on the paternally inherited chromosome. Gains present on chromosomes 5, 10, 13, and 21 are each indicated with a pink dot representing duplication on the maternally inherited chromosome. The text adjacent to each dot denotes the size (in Mb) of each *dnCNV*. **c** Pedigree of *MdnCNV* family (top) with aCGH result for each *dnCNV* region. Parental origin of each chromosome harboring a *dnCNV* in the proband is indicated by a "P" (paternal) or "M" (maternal) on each array



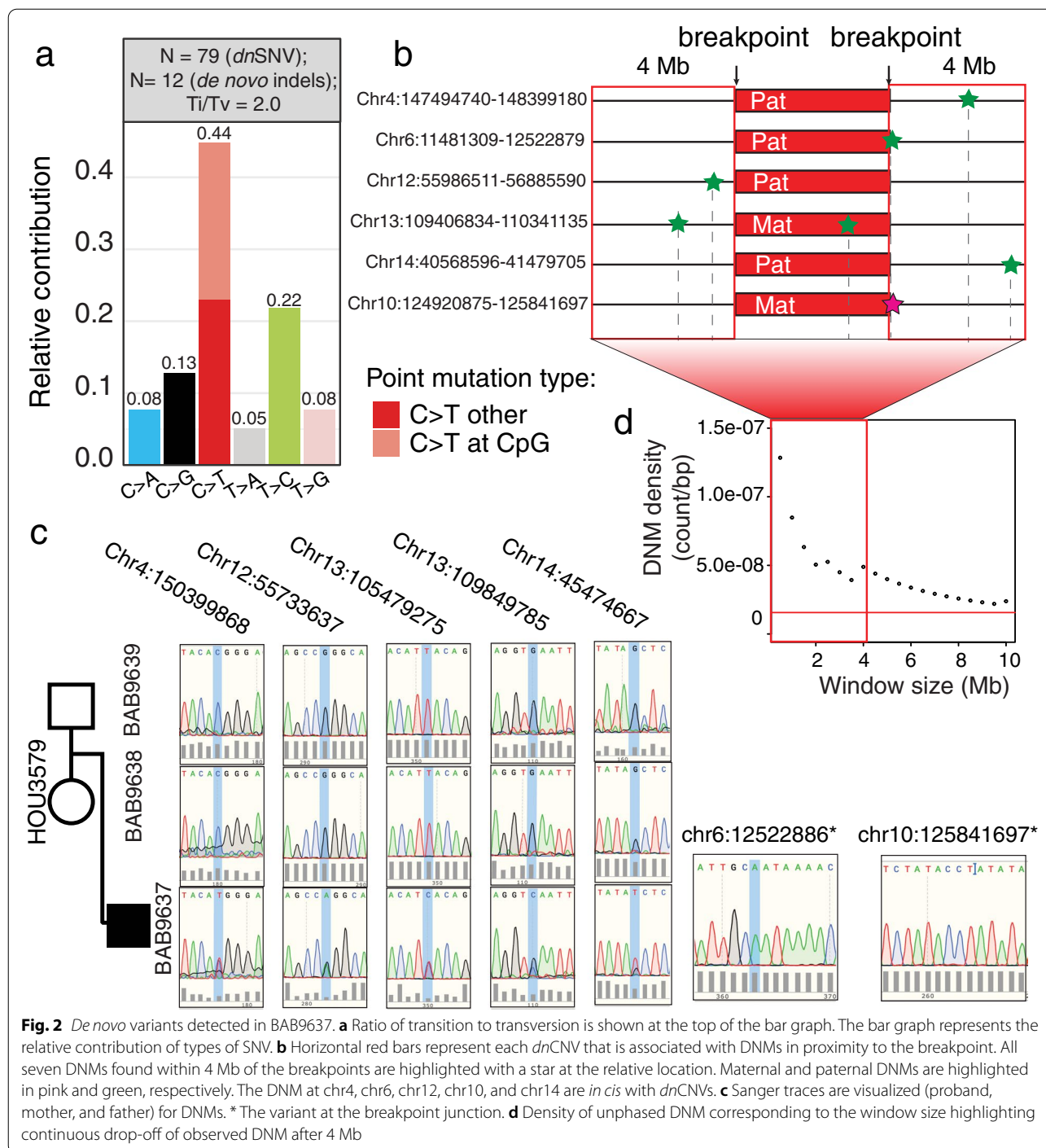


Fig. 2 *De novo* variants detected in BAB9637. **a** Ratio of transition to transversion is shown at the top of the bar graph. The bar graph represents the relative contribution of types of SNV. **b** Horizontal red bars represent each *dnCNV* that is associated with DNMs in proximity to the breakpoint. All seven DNMs found within 4 Mb of the breakpoints are highlighted with a star at the relative location. Maternal and paternal DNMs are highlighted in pink and green, respectively. The DNM at chr4, chr6, chr12, chr10, and chr14 are *in cis* with *dnCNVs*. **c** Sanger traces are visualized (proband, mother, and father) for DNMs. * The variant at the breakpoint junction. **d** Density of unphased DNM corresponding to the window size highlighting continuous drop-off of observed DNM after 4 Mb

leukocyte-derived DNA, which will change the expectation of variant allele fractions (VAFs), e.g., somatic mutation arising during first cell division will have expected VAFs of 25%. The *de novo* substitutions were classified into potential germline mutation, or post-zygotic mutation based on the variant read to total read ratio (Fig. 3a, b, and “Methods”). The number of

potential germline substitutions in *MdnCNV* families appears to be comparable ($p=0.1$, F-test) to control families with an average paternal age effect of 1.9 (95% confidence interval 1.32–2.54) (Fig. 3c, d). However, the proportion of potential post-zygotic substitutions appears to be higher (z -test, $p=0.004$) in *MdnCNV* (8.0%, $n=36$) versus control families (3.2%, $n=11$).

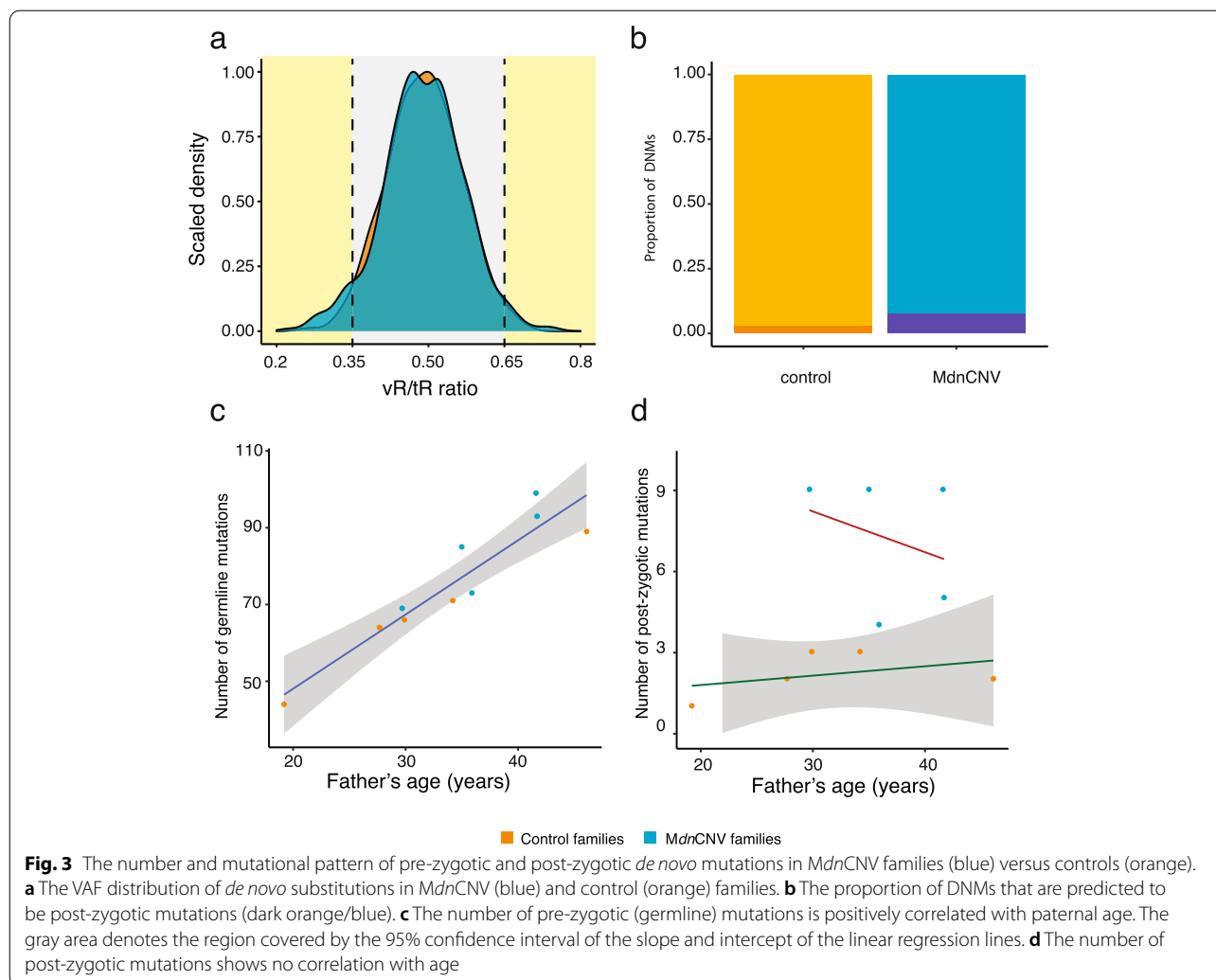
Table 1 Sample information and *de novo* substitution calls

Family	MdnCNV cases						Anonymized control cases											
	HOU1209 ^a	HOU1404 ^a	HOU3425 ^a	HOU3579	BAB9637 (M)	mCNV7 ^a	Average (95 CI)	Fam1	Fam2	Fam3	Fam4	Fam5	Average (95 CI)	P1	P2	P3	P4	P5
Individual (gender)	BAB3097 (F)	BAB3596 (M)	mCNV3/BAB9484 (M)	BAB9637 (M)	mCNV7 (F)	mCNV7 (M)	Average (95 CI)	Fam1	Fam2	Fam3	Fam4	Fam5	Average (95 CI)	P1	P2	P3	P4	P5
Parental age of conception (years)	29.4	37.0	37.8	36.9	35	35.9	35.2 (31.0–39.5)	17.2	30.3	41	28.4	32.3	29.8 (19.2–40.5)					
	29.7	41.7	41.6	35.9	37	35.9	37.2 (31.0–43.3)	19.2	29.9	46.1	27.7	34.2	31.4 (19.2–43.7)					
Number of <i>de novo</i> substitution mutations ^b	75	94	102	74	89	74	93.2 (75.3–111.1)	47	69	98	64	72	72.2 (48.8–95)					
	9	5	9	4	9	4	7.2 (4.1–10.3)**	1	3	2	2	3	2.2 (1.2–3.2)					
Total	84	99	111	78	98	78	93.2 (75.3–111.0)	48	72	100	66	75	72.2 (48.9–95.5)					
Ti:Tv ratio	1.8	2.1	1.6	2.0	2.3	2.0	2.2 (1.62–2.30)	2.4	2.4	1.1	3.1	2.0	2.2 (1.29–3.1)					

M Male, F Female, SNV Single-nucleotide variant, CNV Copy number variant, CI Confidence interval, ** $p < 0.01$; Ti Transition, Tv Transversion

^a MdnCNV families first reported in Liu et al.[9]

^b Variants at the breakpoint junction are not included for the comparison



The paternal age effect on the number of potential post-zygotic variants was not significant for either group.

Mutation pattern analysis for DNMs

We cataloged 466 *de novo* substitutions into seven different mutation types, including the six possible single base-pair substitutions and one category representing CpG deamination. The mutation pattern of germline substitutions in *MdnCNV* families does not appear to be different from controls, with ~40% of the germline mutations being C > T transition variants (Additional file 1: Figure S5). This is consistent with the elevated rate of spontaneous deamination of 5-methyl-cytosine, which occurs at CpG dinucleotides [32].

A higher-resolution mutation substitution pattern analysis was performed on genome-wide *dnSNVs* to investigate the contribution of validated mutational signatures extracted from somatic mutation analysis of the cancer genome [12]. We found that SBS5 and SBS1 explain

the majority of genome-wide *dnSNVs* in all the control and three of *MdnCNV* probands (BAB9484, BAB9637, and mCNV7, Fig. 4d, Additional file 2: Table S2). In contrast, the other mutational signatures (SBS10b, SBS26, and SBS39) were observed in two *MdnCNV* cases (BAB3097 and BAB3596) (Fig. 4d). To exclude potential context bias around the *dnCNV* region, e.g., C > T at CpG for TCG context, mutation signatures were reassessed on *dnSNV* not present within *dnCNV* and 1 Mb distance flanking the breakpoints. After reassessment, SBS1, SBS26, and SBS39 are still associated with BAB3596. SBS39, SBS10b, and SBS37 instead of SBS39, SBS10b, and SBSB26 are associated with BAB3097 (Fig. 4d and Additional file 1: Figure S6), which suggests a nonspecific association of SBS26 with BAB3097.

Rare variant analyses in the maternal genome identified deleterious variants in three genes involving DNA repair pathways from three *MdnCNV* families (HOU1209, HOU3425, and HOU3579, Fig. 4a, b and c).

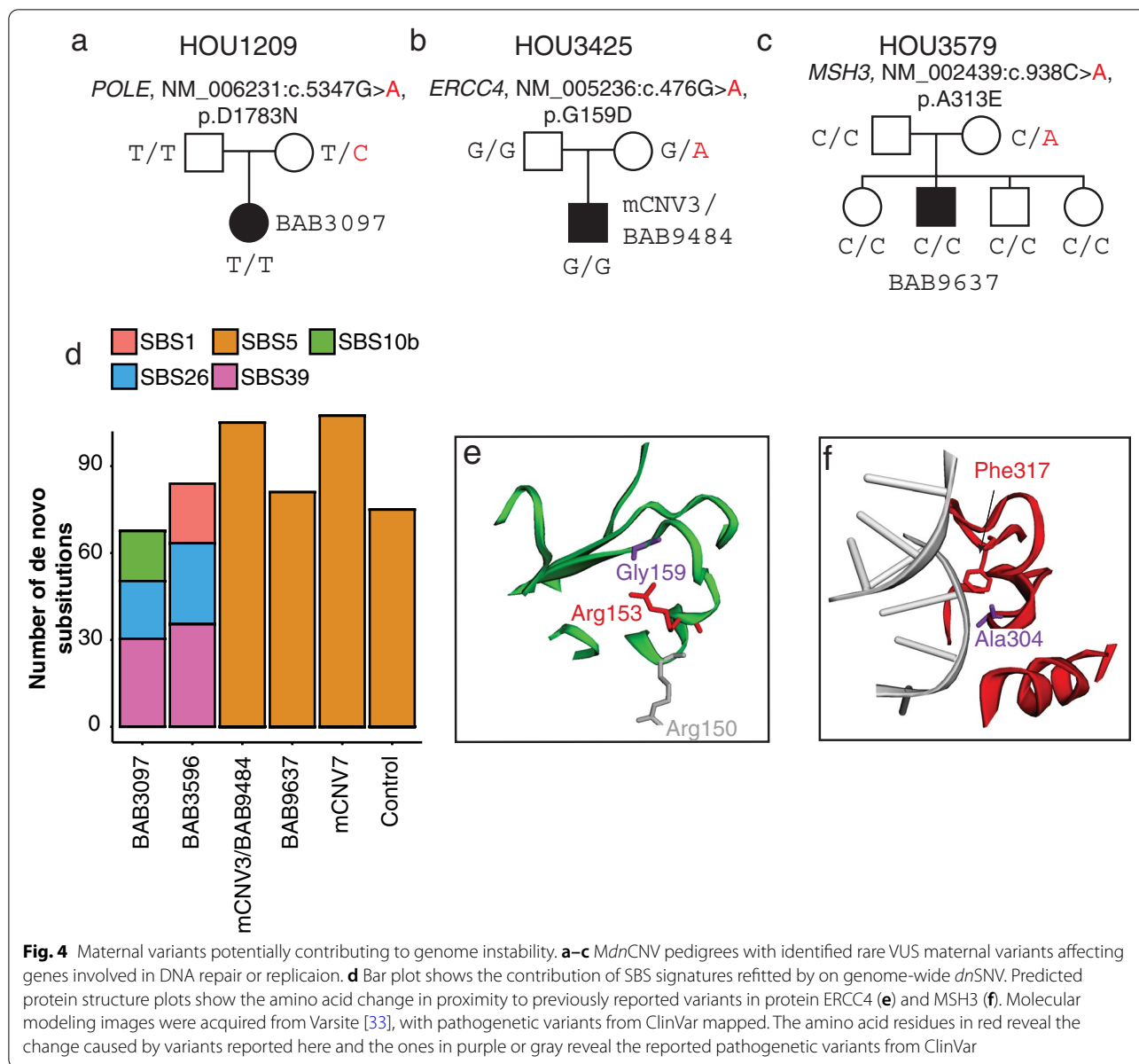


Fig. 4 Maternal variants potentially contributing to genome instability. **a–c** *MdnCNV* pedigrees with identified rare VUS maternal variants affecting genes involved in DNA repair or replication. **d** Bar plot shows the contribution of SBS signatures refitted by on genome-wide *dnSNV*. Predicted protein structure plots show the amino acid change in proximity to previously reported variants in protein ERCC4 (**e**) and MSH3 (**f**). Molecular modeling images were acquired from Varsite [33], with pathogenic variants from ClinVar mapped. The amino acid residues in red reveal the change caused by variants reported here and the ones in purple or gray reveal the reported pathogenic variants from ClinVar

The *POLE* variant (NM_006231:exon39:c.5347G > A:p.D1783N) identified in HOU1209 family (Fig. 4a) is ultrarare in a population database (rs149893630, gnomAD 0.001%). In silico analysis supports that this missense variant has a deleterious effect on protein structure/function (Polyphen2: Probably Damaging; SIFT: Deleterious; CADD v1.6=29.4). We also identified variants in *ERCC4* and *MSH3* from two other *MdnCNV* families (HOU3425 and HOU3579, Fig. 4b,c). Both variants (*ERCC4*:NM_005236:exon3:c.476G > A:p.G159D and *MSH3*:NM_002439:exon6:c.9

38C > A:p.A313E) are absent from the gnomAD database and are predicted to be pathogenic (Polyphen2: Damaging; Damaging; SIFT: Deleterious, Deleterious; CADD v1.6=29.5 and 33.0, respectively). The amino acid residue at both sites are highly conserved from the 161-aligned and 144-aligned protein sequence based on predictions from the tool Varsite [33]. The mutated residues are in proximity to the reported sequences with predicted functional consequences based on 3D protein models (Fig. 4e,f) from Varsite [33] and MichelaNglo [34].

Phenotypic variability derived from variable regions affected by *dnCNV* in the *MdnCNV* cohort

While probands described with the *MdnCNV* phenomenon have a similar molecular finding on analysis for CNV in their genomes, their phenotypic features observed at clinical evaluation are variable. Within the cohort of five individuals with *MdnCNV* phenotype, three patients have detailed clinical information available (Supplementary text) for genotype and phenotype analysis. To discern whether phenotypic variability results from the variable regions of the genome affected by the *MdnCNV* phenomenon, HPO-based evaluation was also performed on the three *MdnCNV* probands (BAB9637, mCNV3/BAB9484, and BAB3097).

Concerning BAB9637, we classified the *de novo* duplication encompassing *NSDI* associated with Sotos syndrome (MIM#117550) as a pathogenic variant, based on the most recent consensus recommendation of the American College of Medical Genetics and Genomics (ACMG) (Table 2) [35]. The remaining *dnCNVs* (7/8) were classified as variants of unknown significance (VUS). To investigate the contribution of the other *dnCNV* encompassing genes to patient phenotype, we performed Lin semantic similarity analysis of BAB9637's phenotype to OMIM/Orphanet HPO annotated gene and disease-associated phenotypes. The Lin semantic similarity scores [27] suggest that, of the genes encompassed by *dnCNV* regions, *NSDI* and *SMARCC2* were the two with the highest phenotypic similarity score (0.60 and 0.59, respectively) to the proband's phenotype (Additional file 1: Table S6). We compared the phenotype similarity of BAB9637 with previously reported probands with only *NSDI* variants (30 probands with *NSDI* duplication, 30 probands with *NSDI* deletion/LoF variant) or only *SMARCC2* variants. Three clusters were observed, one consisting of all 30 included *NSDI* deletion/LoF probands, the second of 25/30 (81%) of reported *NSDI* duplication probands, and the third containing 16/16 *SMARCC2* LoF probands, 5/30 of *NSDI* duplication probands, and BAB9637 (Fig. 5a).

We evaluated whether the observed phenotypes of BAB9637 are better explained by a combinatorial effect of two or more affected genes, i.e., dual molecular diagnosis or MPV, multilocus pathogenic variation. The combination of *NSDI* and *SMARCC2* yielded the highest similarity score (0.64) among all pairwise gene combinations (Fig. 5b). Compared with a single gene model, a dual molecular diagnosis model improved the phenotypic similarity score by >5%. The increase in phenotypic similarity score was not substantial in the 3rd, the 4th, or the 5th gene (~1%) compared to the dual molecular diagnosis model (Additional file 1: Table S6). A review of the phenotypes associated with *NSDI* and *SMARCC2*

in grid format reveals that their phenotypic spectrums largely overlap (Fig. 5c). The grid visualization also highlights the presence of phenotypes in the proband that has predominantly or only been observed in *NSDI* probands (e.g., absent/small foot bones) or in *SMARCC2* probands (e.g., thick eyebrows, inguinal hernia; Fig. 5c). The combination of phenotypic contributions from defects caused by both *NSDI* and *SMARCC2*, therefore, offers the most parsimonious explanation to account for the overall phenotypic presentation in the patient, supporting a multilocus pathogenic variation (MPV) model of blended phenotypic traits caused by perturbation of genes at both loci to constitute the proband's phenotype.

For the BAB3097 *MdnCNV* case, two *de novo* duplication CNV, one (17p12p11.2) with two genes within a contiguous duplication, *RAI1* and *PMP22* associated with Yuan-Harel-Lupski Syndrome (YUHAL; MIM#616652) [36], and the other (1p36.22p36.13) encompassing established haploinsufficiency gene *SPEN*, meet ACMG criteria for pathogenicity (pathogenic/likely pathogenic) and appear to be the clinically relevant genes within these CNV intervals (Table 2). *RAI1* has the highest similarity score (Lin similarity score 0.52), and *PMP22* ranks 11 (Lin similarity score 0.39) among *dnCNV* encompassed genes (Additional file 1: Table S6). The proband phenotype was analyzed for phenotypic similarity with 17 reported YUHAL cases and OMIM diseases associated with either *RAI1* or *PMP22*. Three clusters were observed, one consisting of 12/17 YUHAL probands, the second of 5/17 of reported YUHAL probands and BAB3097, and the last one containing *PMP22* associated neurological diseases (Additional file 1: Figure S7a). The phenotypic grid suggests 7/11 of BAB3097's observed phenotype matches with YUHAL associated phenotypes reported in Yuan et al. (Additional file 1: Figure S7b) [36]. Additional genes with a high phenotypic similarity score include *FLCN* (Lin similarity score 0.50, ranked second) located at 17p12p11.2 and *SPEN* (Lin similarity score 0.45, ranked fourth) at 1p36.22p36.13 (Additional file 1: Table S6). Among all dual molecular diagnosis combinations, 13 have more than 5% improvement of similarity scores over single gene similarity scores. Of those 13 combinations, all have at least one gene within the two regions (17p12p11.2 and 1p36.22p36.13), and 8/13 are made up exclusively of genes within the same regions (Additional file 1: Table S6).

For mCNV3/BAB9484, we classify the *de novo* duplication at 3q26.32 as likely pathogenic based on ACMG guidelines (Table 2). *TBLXR1* was the only coding gene at the duplication region and had the highest phenotypic similarity score (Lin semantic similarity score=0.50) among all *dnCNV* encompassed genes. The second highest gene is *EXT2* (Lin similarity score=0.39). Of all dual

Table 2 Genes mapping to the duplicated genomic region

Sample	Locus	dnCNV Coordinates(GRCh38)	dnCNV type	OMIM disease genes (associated trait MIM#) mapping in duplicated region	Number of genes(pLI > 0.9)	Total number of genes overlapping duplication region	ACMG classification evidence*	ACMG classification
BAB9637	4q31.22q31.23	chr4:147494740-148399180	DUP	EDNRA (#616367, AD); NR3C2 (#177735, AD)	2	10	1A, 2J, 3A, 4D	VUS
BAB9637	5q35.2q35.3	chr5:176449583-177376826	DUP	SNCB (#127750, AD); NSD1 (#117550, AD)	3	23	1A, 2A	Pathogenic
BAB9637	6p24.2p24.1	chr6:11481309-12522879	DUP	EDN1 (#612798, AD); #615706, AR)	1	10	1A, 3A, 4D	VUS
BAB9637	10q26.13q26.2	chr10:124920875-125841697	DUP	UROS (#263700, AR); MMP21 (#616749, AR)	1	16	1A, 3A, 4D	VUS
BAB9637	12q13.2q13.3	chr12:55986511-56885590	DUP	MIP (#615274, AD), ERBB3 (#133180, AD; #607598, AR), SMARCC2 (#618362, AD), RPS26 (#613309, AD), SLC39A5 (#615946, AD), SUOX (#272300, AR), STAT2 (#618886, AR; #616636, AR)	8	40	1A, 2H, 3B, 4B	VUS
BAB9637	13q33.3q34	chr13:109406834-110341135	DUP	COL4A1 (#180000, AD; #611773, AD; #175780, AD; #618564, AD), COL4A2 (#614483, AD), IRS2 (#125853, AD)	1	8	1A, 3A, 4D	VUS
BAB9637	14q21.1	chr14:40568596-41479705	DUP		0	0	1B	VUS
BAB9637	21q21.3	chr21:28158347-29192300	DUP		1	12	1A, 3A, 4D	VUS

Table 2 (continued)

Sample	Locus	dnCNV Coordinates(GRCh38)	dnCNV type	OMIM disease genes (associated trait MIM#) mapping in duplicated region	Number of genes(pLI > 0.9)	Total number of genes overlapping duplication region	ACMG classification evidence*	ACMG classification
BAB3097	1p36.22p36.13	chr1:10115497-16283149	DUP	KIF1B (#118210, AD; #171300, AD; #256700), PEX14 (#614887, AR), TARDBP (#612069, AD), MASP2 (#613791, AR), MITOR (#616638, AD), UBIAD1 (#121800, AD), MAD2L2 (#617243, AR), MTHFR (#236250, AR), CLCN6 (#619173, AD), NPPA (#612201, AD; #615745, AR), PLOD1 (#225400, AR), MFN2 (#609260, AD; #617087, AR; #601152, AD), VPS13D (#607317, AR), CELA2A (#618620, AD), SPEN (#619312, AD), CLCNKA (#613090, DR), CLCNKB (#607364, AR; #613090, DR), EPHA2 (#116600, AD)	13	167	1A, 3C, 4C	Likely Pathogenic
BAB3097	3q13.33q21.1	chr3:122157406-123113479	DUP	CASR (#239200, AD/AR; #601198, AD; #145980, AD), CSTA (#607936, AR)	19	2	1A, 3A, 4D	VUS
BAB3097	5p12	chr5:44375961-44815730	DUP	FGF10 (#180920, AD; #149730, AD)	0	2	1A, 2J, 3A, 4D	VUS
BAB3097	5q33.3q34	chr5:158887731-164722046	DUP	IL12B (#614890, AR), GABRB2 (#617829, AD), GABRA1 (#615744, AD), GABRG2 (#618396, AD; #607681, AD)	5	42	1A, 3A, 4D	VUS
BAB3097	9p13.3	chr9:33492358-34725916	TRP	UBAP1 (#618418, AD); MYORG (#618317, AR), DNAAF1 (#244400, AR), SIGMAR1 (#614373, AR; #605726, AR), GALT (#230400, AR), IL11RA (#614188, AR)	4	53	1A, 3C, 4D	VUS

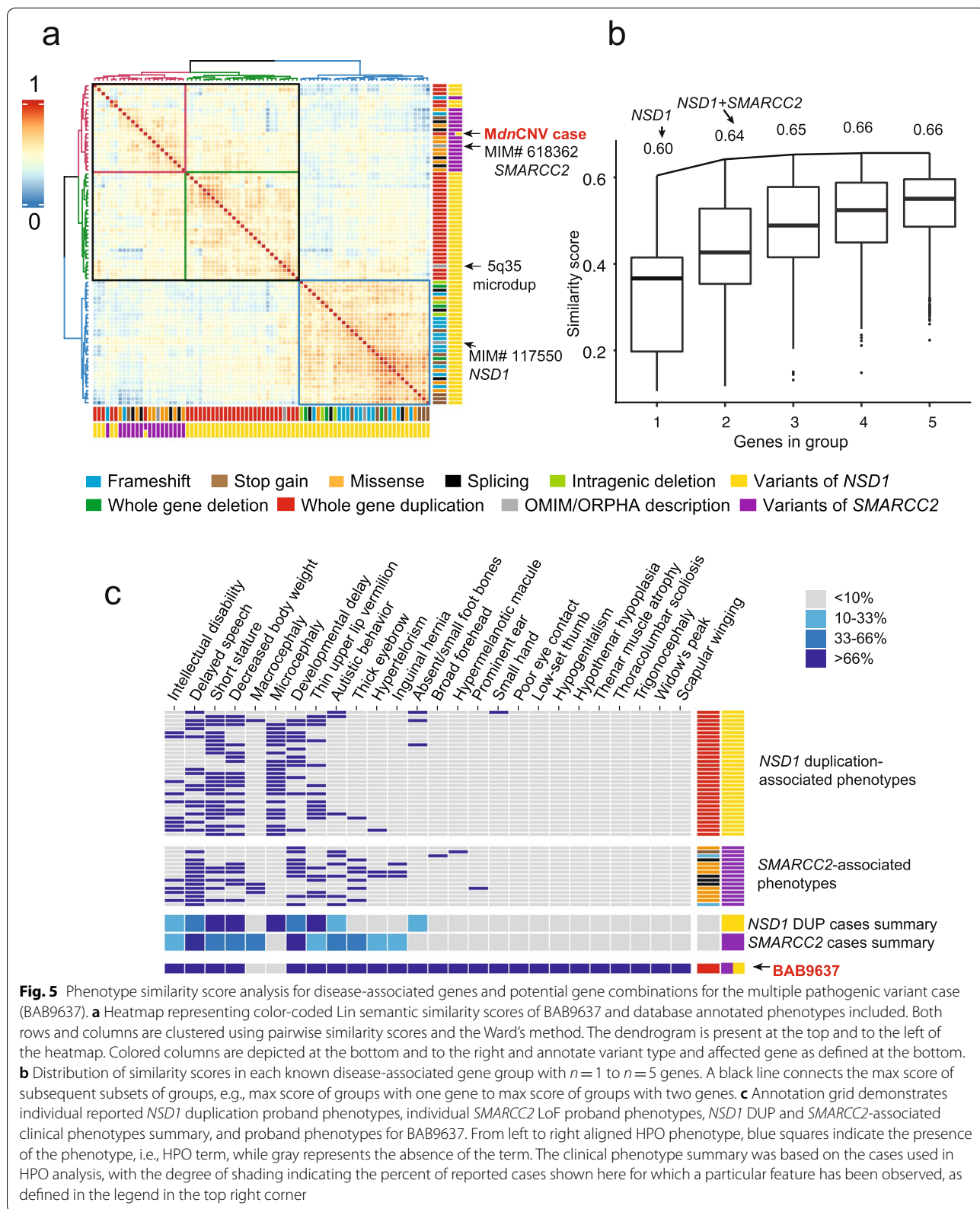
Table 2 (continued)

Sample	Locus	dnCNV Coordinates(GRCh38)	dnCNV type	OMIM disease genes (associated trait MIM#) mapping in duplicated region	Number of genes(pLI > 0.9)	Total number of genes overlapping duplication region	ACMG classification evidence*	ACMG classification
BAB3097	17p12p11.2	chr17:11915997-17892664	DUP	DNAH9 (#618300, AR), MYOCD (#618719, AD), ELAC2 (#615440, AR), COX10 (#619046, AR), PMP22 (#139393, AD; #118220, AD; #118300, AD; #145900, AD; #162500, AD; #180800, AD), TTC19 (#615157, AR), PIGL (#280000, AR), TNFRSF13B (#240500, AD/AR), FLCN (#135150, AD; #173600, AD), RAI1 (#182290, AD), SREBF1 (#619016, AD; #158310, AD)	7	110	1A, 2A	Pathogenic
BAB3097	22q13.31p13.32	chr22:47979382-48288823	DUP	SLC35D1 (#269250, AR), WLS (#619648, AR), RPE65 (#204100, AR; #613794, AR; #618697, AD), CTH (#219500, AR), TNN3K (#616117, AD), ACADM (#201450, AR), PIGK (#618879, AR), NEXN (#613122, AD; #613876, AD)	0	1	1A, 3A, 4D	VUS
mCNV3/BAB9484	1p31.3p31.1	chr1:66885559-77949895	DUP	COA6 (#616501, AR), IRF2BP2 (#617765, AD), GGP51 (#619518, AR), TBCE (#617207, AR; #241410, AR; #244460, AR), B3GALNT2 (#615181, AR)	9	108	1A, 3C, 4D	VUS
mCNV3/BAB9484	1q42.2q42.3	chr1:233450789-235471180	DUP	ASPRV1 (#146750, AD), TIA1 (#619133, AD; #604454, AD/AR), FIGLA (#612310, AD), ATP6V1B1 (#267300, AR), MCEE (#251120, AR)	1	35	1A, 3B, 4D	VUS
mCNV3/BAB9484	2p13.3	chr2:69512973-71153026	DUP	TBL1XR1 (#616944, AD; #602342, AD)	2	44	1A, 3B, 4D	VUS
mCNV3/BAB9484	3q26.32	chr3:176661565-177473432	DUP	SECISBP2 (#609698, AR)	1	8	1A, 2A, 3A, 4C	Likely Pathogenic
mCNV3/BAB9484	9q22.2	chr9:89241202-90787598	DUP	EXT2 (#133701, AD; #616682, AR), ALX4 (#613451, AR; #609597, AD; #615529, AD)	2	38	1A, 3B, 4D	VUS
mCNV3/BAB9484	11p12p11.2	chr11:42871836-44852545	DUP		2	25	1A, 2H, 3B, 4D	VUS

Table 2 (continued)

Sample	Locus	dnCNV Coordinates(GRCh38)	dnCNV type	OMIM disease genes (associated trait MIM#) mapping in duplicated region	Number of genes(pLi > 0.9)	Total number of genes overlapping duplication region	ACMG classification evidence*	ACMG classification
mCNV3/BAB9484	16q22.2	chr16:71219688-71768356	DUP	HYDIN (#608647, AR), TAT (#276600, AR), AP1G1 (#619467, AD)	1	16	1A, 3A, 4D	VUS
mCNV3/BAB9484	20q13.33	chr20:61800345-63644611	DUP	OSBP12 (#616340, AD), GATA5 (#617912, AD/AR), COL9A3 (#600969, AD), SLC17A9 (#616063, AD), CHRNA4 (#600513, AD), KCNQ2 (#613720, AD), #121200, AD), EEFLA2 (#616409, AD; #616393, AD)	4	15	1A, 3A, 4D	VUS

pLi probability of being Loss-of-function intolerant, AD autosomal dominant, AR autosomal recessive, DR digenic recessive, ACMG American College of Medical Genetics and Genomics, OMIM Online Mendelian Inheritance in Man. *Evidence code based on ACMG consensus recommendation; DUP duplication, TRP Triplication



molecular diagnosis combinations, three have more than 5% improvement of similarity score over a single gene (Additional file 1: Table S6). The phenotype grid suggests 3/10 exact match of *TBLIXR1* associated terms, including hypertelorism, brachycephaly, and wide intermamillary distance (Additional file 1: Figure S8).

Discussion

Our study utilized multimodal genomic approaches to investigate *de novo* genomic rearrangements in an *MdnCNV* family, characterize the mutational event that instigated *MdnCNV* across the genome, identify *de novo* SNV genome-wide, phase CNV and SNV haplotypes, and explore potential driver genes contributing to the observed clinical phenotype. Accurately capturing structural variants and complexities generated during CNV mutagenesis, including novel DNA rearrangement junctions or DNA break/join-points and other SNV mutational signatures of CNV mutagenesis, is challenging given the length limit of sequencing reads in SR genome sequencing. Genome-wide ascertainment of *dnCNVs*, breakpoint junction sequence, and *dnSNVs* were enabled by implementing both LR and SR genome sequencing. LR sequencing, either PacBio [14] or Nanopore as shown here, allows direct phasing of variants multiple kilobases apart, which in turn allows direct observation of *dnSNV in cis* with breakpoint junctions.

The average size of tandem duplication observed in the newly identified *MdnCNV* individual is around 1 Mb, consistent with the observation in the five reported *MdnCNV* individuals [4]. The size is also within a similar size range “window” of replication domains [37] and topologically associating domains (TAD) [38]. Recent study suggests the replication domain boundary is associated with TAD [39]. The size of tandem duplication can be limited within the boundary of the genome organization, e.g., the three-dimensional genome folding and accessibility of DNA during zygotic development. Further analysis on the dynamics of chromatin architecture during zygote development is warranted to address potential influence or constraints on rearrangement size.

We postulate that the CNV generating mechanism could be MMBIR, based on the shared characteristics of microhomology/microhomeology at breakpoint junctions, complexity in the form of associated indels, and the increased occurrence of base substitutions and indels within 4 Mb of junctions. MMBIR, a form of break-induced replication, occurs when a replication fork has collapsed/stalled and restarted. Alternatively, the unrepaired DNA nicks could result in a collapsed fork that is resolved by a mixed NHEJ/MMBIR mechanism, e.g., restart-bypass [40]. Regardless of which mechanism(s) are involved, we suggest that there were multiple

broken replication forks in a single zygotic cell and that the *MdnCNV* event, therefore, may have resulted from cell-wide replication stress, such as energy or substrate unavailability that resulted in multiple broken replication forks.

We found that the mutation rate for *dnCNV* and substitution was elevated in five *MdnCNV* families. The post-zygotic mutational events happened at the early development stage, e.g., first cell division has a VAF of 10–35% [41]. The mutation rate during early embryonic development is higher than in germline cells, expecting 2–3 substitutions per generation [41]. The post-zygotic substitution rate in *MdnCNV* families is three times higher than the rate in control (z -test, $p=0.004$, Table 1). The mechanism(s) causing the CNV mutator phenotype is thought to be due to a transient mutagenesis event restricted to the peri-zygotic stage of development [4]. We suspect the mechanism(s) could also lead to SNV hypermutation limited to the peri-zygotic period. However, high-depth genome sequencing is required for the estimation of mosaicism accurately and further supports this hypothesis.

The *dnSNV* mutational pattern and rare variant analysis suggest multiple mechanisms contributing to the transient peri-zygotic genome instability causing the *MdnCNV* phenomenon. One of the mechanisms could be that non-inherited variants in the maternal genome affect zygotic genome integrity, whereby maternal mRNA stored in the oocyte impacts the first few cell divisions during embryonic development. Rare variant analyses identified maternal variants in three DNA repair genes *POLE*, *ERCC4*, and *MSH3* with predicted deleterious effects on the function that could contribute to peri-zygotic genome instability. The gene *POLE* encodes the catalytic subunit of polymerase ϵ which plays a major role in the DNA replication [42]. The *POLE* variant identified in family HOU1209 is located in the C-terminal structure of the subunit which is essential for replisome assembly and checkpoint activation [43, 44]. The maternal variants identified in family HOU3425 (*ERCC4*, NM_005236:c.476G>A, p.G159D) and HOU3579 (*MSH3*, NM_002439:c.938C>A, p.A313E) may contribute to replication stress through different mechanisms. *ERCC4* (MIM#133520, also known as XPF) encodes the endonuclease catalytic subunit that is involved in nucleotide excision repair (NER) and removes DNA interstrand crosslinking damage [45, 46]. The interstrand crosslink can prevent DNA strand separation and physically block DNA replication and transcription, leading to genomic instability. The mutated residue (*ERCC4*, NM_005236:c.476G>A, p.G159D) is near two reported functional residues that are relevant to the crosslink repair activity of *ERCC4* (Fig. 4e).

The nearest one (rs121913050, p.R153P), located 2.2 Å away from the mutated residue, is classified as pathogenic in ClinVar and causes XFE progeroid syndrome (MIM#610965) in a homozygous state [47, 48]. The second variant (rs145402255, p.R150C), located 10.8 Å away from the mutant residue is classified as likely pathogenic in ClinVar. In vitro cell modeling suggests the variant (rs145402255, p.R150C) can mildly disrupt the inter-strand crosslink repair activity [49]. *MSH3* encodes a protein that forms a heterodimer with *MSH2* that is responsible for mismatch repair (MMR) and double-stranded DNA repair [50, 51]. In summary, these variants may represent genetic modifiers rather than causative drivers that may contribute to the *MdnCNV* phenomenon. Additionally, 4/5 *MdnCNV* families (Table 1) were of advanced parental age (>35 years old) at the time of conception, which may have reduced the capacity of DNA repair in oocytes and therefore have a contributory effect on the genomic stability of the zygote.

Mutational signature analysis can be used to decipher the potential mutational processes underlying individual cancer or germline hypermutation [52, 53]. A recent study has revealed genetic and environmental contributions to the germline *dnSNV* hypermutation [53]. Our study explored the utility of mutational signature analysis to decode potential mutational processes in the context of *dnCNV* hypermutation. However, further studies are still warranted to understand the mutational process(es) during the peri-zygotic development stage. Mutational signature analysis on embryonic somatic mutations (SNVs and CNVs) may help solve the puzzle. Additionally, further studies are needed to confirm mutational signatures within certain genes or allele-specific effects.

Reciprocal copy number changes in dosage-sensitive gene loci can manifest traits on the opposite ends of a phenotypic spectrum, a phenomenon known as mirror traits [54]. The quantitative trait for head size, or occipital frontal circumference (OFC), illustrates this concept: reciprocal CNVs at multiple loci can drive mirror trait expression manifesting as large (macrocephaly) or small (microcephaly) head size [54–56]. Semantic similarity analysis using HPO terms can quantify the similarity of matching phenotype, therefore objectively teasing out the contribution of genes within *dnCNV* regions. The similarity score correctly ranked the established genes in the *dnCNV* region and suggested additional genes from the other regions contributing to two of the *MdnCNV* cases. Quantitative analyses of the clinical phenotypes in BAB9637 versus known disease genes mapping within the duplications implicate *NSDI* as a triplosensitivity trait locus that contributes to the clinical phenotype observed. The 5q35 microdeletion

causing haploinsufficiency of *NSDI* has been associated with Sotos syndrome (MIM#117550). The characteristic clinical features of Sotos syndrome include overgrowth, characteristic facial dysmorphisms, intellectual disability (ID), developmental delay (DD), and macrocephaly. The proband (BAB9637) has overlapping features, including DD and ID. However, regarding the quantitative traits of head circumference and height, the proband (lower-than-average head circumference [$Z = -0.62$]; short stature [$Z = -3.01$]) with a duplication encompassing *NSDI* lies on the opposite end of the phenotypic spectrum compared to individuals with a diagnosis of Sotos syndrome. Furthermore, the clinical presentation of our proband, which includes DD/ID, and short stature, is consistent with that of 31 affected individuals previously reported across multiple studies [57] to have a *de novo* or familial duplication of the genomic region whose deletion is commonly associated with the Sotos syndrome (Fig. 5, Additional file 1: Figure S9).

The presence of two highly similar clusters for *NSDI* duplication and *SMARCC2*, and their separation from a more dissimilar *NSDI* deletion/LoF cluster, highlights the shared phenotypic trait between *NSDI* duplication and *SMARCC2* associated phenotypes. The contribution of *NSDI* does not seem to explain all phenotypes observed in the proband, e.g., scoliosis and craniofacial features. Haploinsufficiency of *SMARCC2* has been associated with Coffin-Siris syndrome 8 (MIM#618362). *SMARCC2* duplication is ultrarare, less than 0.0001 in one control study [58], and absent in the personal genomes of neurotypical individuals from population databases (gnomAD v2.1.1). *SMARCC2* duplication has been reported in three cases (size of duplication <1 Mb) in the *Databases of genomic Variation and Phenotype in Humans using Ensembl Resources* (DECIPHER, <https://www.deciphergenomics.org/>) [59] (Additional file 1: Figure S9). Two genomes with duplications from unrelated patients have a phenotype described, one (DECIPHER patient ID: 343437) in an individual with growth delay and ID, the second duplication (DECIPHER patient ID: 260552) inherited from a parent who has a similar phenotype, including hypertelorism, hypospadias, broad thumb, delayed cranial suture closure, hypotonia, and ID. Data on segregation of duplication variants in DECIPHER individuals was not available.

The potential molecular diagnoses underlying BAB3097's phenotype highlight another case where *de novo* CNV at more than one locus contributes to disease pathobiology. Contiguous gene duplication encompassing *RAI1* and *PMP22* has been previously described in 17 patients with YUHAL syndrome [36]. Renal phenotypes were observed in 4/17 of patients with

Yuan-Harel-Lupski (YUHAL) syndrome, and while a definitive gene within the duplication interval was not associated with renal phenotypes, *FLCN* was suggested to be a potential contributor. In addition to the duplication at this locus, our analysis suggests duplication at 1p36.22p36.13 may also contribute to the phenotype, with *SPEN* as the potential driver gene. The gene *SPEN* is located at the 1p36 deletion syndrome critical region. Furthermore, truncated variants at *SPEN* suggest the haploinsufficiency of *SPEN* associated with neurodevelopment phenotype, congenital heart defects, and facial dysmorphism [60]. The whole gene duplication of *SPEN* was absent from DGV and gnomAD.

Further study of the phenotypic effect of *SMARCC2* and *SPEN* duplication in more patients, rather than deletion, is necessary to understand dosage sensitivity (i.e., triplosensitivity) at these loci; however, these data in aggregate support the contention that the phenotype of the proband is a blended overlapping phenotype driven by multilocus pathogenic variation (MPV) [21, 61], i.e., duplication of the *NSDI* and *SMARCC2* loci, and their associated traits. Our understanding of emerging concepts, such as which genes or loci are dosage-sensitive, whether haploinsufficiency and triplosensitivity traits will be observed for a given dosage-sensitive gene, and the correlation between dosage-sensitive genes and mirror traits is continuing to evolve with human genetics and genomics studies.

While semantic similarity analysis with patient phenotypes can objectively tease out the contribution of genes within *dnCNV* regions, there are some caveats to such analysis. First, the variable depth of phenotypic information could affect the clustering, e.g., the unavailability of nerve conduction studies in BAB9484 affecting phenotypic match to previously reported YUHAL probands which were extensively evaluated clinically [36]. Another caveat is that portions of these proband phenotypes may be due to genes encompassed by CNV that are not yet associated with disease in humans or by other yet unrecognized genetic modifiers/pathogenic SNV contributing to the phenotype. Nevertheless, aggregate data of quantitative phenotypic analysis of *MdnCNV* probands suggests that at least some phenotypic variability is likely explained by dosage changes of genes encompassed by CNV genome-wide in probands. These cases also highlight the possibility of multiple genes, in one case as part of a contiguous gene duplication of *PMP22* and *RAI1* and in another as duplications of *NSDI* and *SMARCC2* at separate loci undergoing *de novo* gains in a single generation to contribute to phenotype manifestation.

Conclusions

Characterization of the *MdnCNV* phenomenon using a multimodal genomic approach revealed insights that the *MdnCNV* mutational event likely occurs in the earliest post-zygotic stages of development—potentially in the pronuclear phase or during the first few cell divisions. Moreover, we show the utility of quantitative phenotypic analysis to identify contributory, disease-associated genes within a background of genome-wide *dnCNVs* and provide evidence for duplications at two genomic loci containing triplosensitive genes that contribute to the patient's blended phenotype.

Abbreviations

aCGH: Array comparative genomic hybridization; *dnCNVs*: *De novo* copy number variants; DNMs: *De novo* Mutations; *dnSNVs*: *De novo* single-nucleotide variants; HPO: Human Phenotype Ontology; MMBIR: Microhomology-mediated break-induced replication; MPV: Multilocus pathogenic variation; NHEJ: Non-homologous end joining; OFC: Occipital frontal circumference; SNPs: Single-nucleotide polymorphisms.

Supplementary Information

The online version contains supplementary material available at <https://doi.org/10.1186/s13073-022-01123-w>.

Additional file 1. Supplementary methods, clinical description of BAB9637, BAB3097, and BAB9484, Table S1, S3, S5, S6, Figure S1-S9.

Additional file 2: Table S2.

Additional file 3: Table S4. *dnSNVs* in the proband (not include the *dnSNV* within 150bp to the breakpoint).

Acknowledgements

We thank the family and collaborators for their participation in this study.

Authors' contributions

Conceptualization: H.D., C.M.G., A.J., J.R.L., P.L., and C.C.; Data curation: S.N.J., C.M.G., J.M.F., M.P., S.J., E.H., B.Y., and H.L.; Formal analysis: H.D., C.M.G., and A.J.; Funding acquisition: J.R.L., C.C., P.J.H., R.A.G., P.L., and J.E.P.; Visualization: H.D., A.J., C.M.G., and J.M.F.; Methodology: C.C., F.J.S., and Z.C.A.; Resources: M.E.C., A.E.S., and J.E.P.; Supervision: C.C., J.R.L., and P.L.; Writing—original draft: H.D.; Writing—review and editing: H.D., A.J., C.M.G., J.R.L., P.L., C.C., and P.J.H. All author(s) read and approved the final manuscript.

Funding

Supported in part by US National Institutes of Health, National Human Genome Research Institute (NHGRI)/National Heart, Lung, and Blood Institute (NHLBI) UM1 HG006542 to the Baylor Hopkins Center for Mendelian Genomics, NHGRI U54 HG003273 and NHGRI UM1 HG008898 to RAG, the NHGRI Genomic Research Elucidates Genetics of Rare disease (GREGoR) consortium U01 HG011758 to JEP, JRL, and RAG. NHGRI K08 HG008986 to JEP; the National Institute of General Medical Sciences (NIGMS R01 GM132589 to CMBC and R01 GM106373 to PH and JRL); and the National Institute for Neurological Disorders and Stroke (NINDS R35 NS105078 to JRL); NHGRI R35HG011311 to P.L.

Availability of data and materials

The data generated or analyzed during this study are included in this published article. The array data has been submitted to GEO (GSE176427) [62]. The variant data of the study are available with ClinVar accession numbers: SCV002576315—SCV002576337.

Declarations

Ethics approval and consent to participate

Written informed consent was obtained from the families of BAB9637, BAB3097, and BAB9484 in the research study. This study was approved by the Institutional Review Board (IRB) at Baylor College of Medicine (protocols H-29697 and H-42680). A waiver of consent was approved by the study for investigation of the other families included in this study because the analysis and publication of the human subject genomics data have been de-identified and present minimal risks to the study subjects. The research activities in this study conformed to the principles of the Helsinki Declaration.

Consent for publication

Written consent was obtained to publish detailed clinical information for the families of BAB9637, BAB3097, and BAB9484. A waiver of consent was approved by the study IRB to publish a de-identified synopsis of the clinical summary of the other families using HPO terms.

Competing interests

Baylor College of Medicine (BCM) and Miraca Holdings have formed a joint venture with shared ownership and governance of Baylor Genetics (BG), which performs clinical chromosome microarray analysis (CMA) and other genomic studies (ES, genome sequencing) for patient/family care. J.R.L. serves on the Scientific Advisory Board of BG. J.R.L. has stock ownership in 23andMe, is a paid consultant for the Regeneron Genetics Center, and is a co-inventor on multiple United States and European patents related to molecular diagnostics for inherited neuropathies, eye diseases, genomic disorders, and bacterial genomic fingerprinting. PL and WB are employees of BCM and derive support through a professional service agreement with BG. MP, EH, and SJ are employees of Oxford Nanopore Technologies and are shareholders and/or share option holders. FJS has multiple travels sponsored by Pacbio and ONT. The remaining authors declare that they have no competing interests.

Author details

¹Department of Molecular and Human Genetics, Baylor College of Medicine, One Baylor Plaza, Houston, TX 77030, USA. ²Medical Scientist Training Program, Baylor College of Medicine, Houston, TX 77030, USA. ³Baylor Genetics Laboratory, Houston, TX 77021, USA. ⁴Seattle Children's Hospital, Seattle, WA 98105, USA. ⁵Human Genome Sequencing Center, Baylor College of Medicine, Houston, TX 77030, USA. ⁶Human Genetics Center, Department of Epidemiology, Human Genetics, and Environmental Sciences, School of Public Health, The University of Texas Health Science Center at Houston, Houston, TX 77030, USA. ⁷Division of Genetics and Metabolism, Department of Pediatrics, University of Texas Southwestern Medical Center, Dallas, TX 75390, USA. ⁸Division of Genetics Diagnostics, Department of Pathology, University of Texas Southwestern Medical Center, Dallas, TX 75390, USA. ⁹McDermott Center for Human Growth and Development, University of Texas Southwestern Medical Center, Dallas, TX 75390, USA. ¹⁰Clinical Institute of Medical Genetics, University Medical Centre Ljubljana, 1000 Ljubljana, Slovenia. ¹¹Medical Faculty, University of Ljubljana, 1000 Ljubljana, Slovenia. ¹²Oxford Nanopore Technologies Inc, New York, NY 10013, USA. ¹³Dan L. Duncan Comprehensive Cancer Center, BCM, Houston, TX 77030, USA. ¹⁴Department of Pediatrics, Baylor College of Medicine, Houston, TX 77030, USA. ¹⁵Texas Children's Hospital, Houston, TX 77030, USA. ¹⁶Pacific Northwest Research Institute, 720 Broadway, Seattle, WA 98122, USA.

Received: 4 March 2022 Accepted: 10 October 2022

Published online: 27 October 2022

References

- Collins RL, Brand H, Karczewski KJ, Zhao X, Alföldi J, Francioli LC, et al. A structural variation reference for medical and population genetics. *Nature*. 2020;581:444–51.
- Belyeu JR, Brand H, Wang H, Zhao X, Pedersen BS, Feusier J, et al. *De novo* structural mutation rates and gamete-of-origin biases revealed through genome sequencing of 2,396 families. *Am J Hum Genet*. 2021;108:597–607.
- Itsara A, Wu H, Smith JD, Nickerson DA, Romieu I, London SJ, et al. *De novo* rates and selection of large copy number variation. *Genome Res*. 2010;20:1469–81.
- Liu P, Yuan B, Carvalho CMB, Wuster A, Walter K, Zhang L, et al. An organ-ismal CNV mutator phenotype restricted to early human development. *Cell*. 2017;168:830–842.e7.
- Köhler S, Gargano M, Matentzoglou N, Carmody LC, Lewis-Smith D, Vasilevsky NA, et al. The human phenotype ontology in 2021. *Nucleic Acids Res*. 2021;49:D1207–17.
- Cheung SW, Shaw CA, Yu W, Li J, Ou Z, Patel A, et al. Development and validation of a CGH microarray for clinical cytogenetic diagnosis. *Genet Med*. 2005;7:422–32.
- Wiszniewska J, Bi W, Shaw C, Stankiewicz P, Kang S-HL, Purlsey AN, et al. Combined array CGH plus SNP genome analyses in a single assay for optimized clinical testing. *Eur J Hum Genet*. 2014;22:79–87.
- Carvalho CMB, Zhang F, Liu P, Patel A, Sahoo T, Bacino CA, et al. Complex rearrangements in patients with duplications of *MECP2* can occur by fork stalling and template switching. *Hum Mol Genet*. 2009;18:2188–203.
- Farek J, Hughes D, Mansfield A, Krashenina O, Nasser W, Sedlazeck FJ, et al. xAtlas: Scalable small variant calling across heterogeneous next-generation sequencing experiments. *bioRxiv*. 2018. p. 295071. Available from: <https://www.biorxiv.org/content/biorxiv/early/2018/04/05/295071>. [cited 2022 Aug 29]
- Eldomery MK, Coban-Akdemir Z, Harel T, Rosenfeld JA, Gambin T, Stray-Pedersen A, et al. Lessons learned from additional research analyses of unsolved clinical exome cases. *Genome Med*. 2017;9:26.
- Blokzijl F, Janssen R, van Bostel R, Cuppen E. MutationalPatterns: comprehensive genome-wide analysis of mutational processes. *Genome Med*. 2018;10:33.
- Alexandrov LB, Kim J, Haradhvala NJ, Huang MN, Tian Ng AW, Wu Y, et al. The repertoire of mutational signatures in human cancer. *Nature*. 2020;578:94–101.
- Patterson M, Marschall T, Pisanti N, van Iersel L, Stougie L, Klau GW, et al. WhatsHap: weighted haplotype assembly for future-generation sequencing reads. *J Comput Biol*. 2015;22:498–509.
- Beck CR, Carvalho CMB, Akdemir ZC, Sedlazeck FJ, Song X, Meng Q, et al. Megabase length hypermutation accompanies human structural variation at 17p11.2. *Cell*. 2019;176:1310–1324.10.
- Zarate S, Carroll A, Krashenina O, Sedlazeck FJ, Jun G, Salerno W, et al. Parliament2: fast structural variant calling using optimized combinations of callers. *bioRxiv*. 2018. p. 424267. Available from: <https://www.biorxiv.org/content/biorxiv/early/2018/09/23/424267>. [cited 2022 Aug 29]
- Sedlazeck FJ, Rescheneder P, Smolka M, Fang H, Nattestad M, von Haeseler A, et al. Accurate detection of complex structural variations using single-molecule sequencing. *Nat Methods*. 2018;15:461–8.
- Cer RZ, Donohue DE, Mudunuri US, Temiz NA, Loss MA, Starner NJ, et al. Non-B DB v2.0: a database of predicted non-B DNA-forming motifs and its associated tools. *Nucleic Acids Res*. 2013;41:D94–100.
- Halldórsson BV, Pálsson G, Stefánsson OA, Jonsson H, Hardarson MT, Eggertsson HP, et al. Characterizing mutagenic effects of recombination through a sequence-level genetic map. *Science*. 2019;363. Available from: <https://doi.org/10.1126/science.aau1043>
- Venkatraman ES, Olshen AB. A faster circular binary segmentation algorithm for the analysis of array CGH data. *Bioinformatics*. 2007;23:657–63.
- Gel B, Serra E. karyoploteR: an R/Bioconductor package to plot customizable genomes displaying arbitrary data. *Bioinformatics*. 2017;33:3088–90.
- Herman I, Jolly A, Du H, Dawood M, Abdel-Salam GMH, Marafi D, et al. Quantitative dissection of multilocus pathogenic variation in an Egyptian infant with severe neurodevelopmental disorder resulting from multiple molecular diagnoses. *Am J Med Genet A*. 2022;188:735–50.
- Zhang C, Jolly A, Shayota BJ, Mazzeu JF, Du H, Dawood M, et al. Novel pathogenic variants and quantitative phenotypic analyses of Robinow syndrome: WNT signaling perturbation and phenotypic variability. *HGG Adv*. 2022;3:100074 (Elsevier BV).
- Lima AR, Ferreira BM, Zhang C, Jolly A, Du H, White JJ, et al. Phenotypic and mutational spectrum of *ROR2*-related Robinow syndrome. *Hum Mutat*. 2022;43:900–18.
- Liu C, Peres Kury FS, Li Z, Ta C, Wang K, Weng C. Doc2Hpo: a web application for efficient and accurate HPO concept curation. *Nucleic Acids Res*. 2019;47:W566–70 (Oxford Academic).

25. Köhler S, Carmody L, Vasilevsky N, Jacobsen JOB, Danis D, Gouridine J-P, et al. Expansion of the human phenotype ontology (HPO) knowledge base and resources. *Nucleic Acids Res.* 2019;47:D1018–27.
26. Greene D, Richardson S, Turro E. ontologyX: a suite of R packages for working with ontological data. *Bioinformatics.* 2017;33:1104–6 (Oxford Academic).
27. Lin D. An information-theoretic definition of similarity. In Proceedings of the 15th International Conference on Machine Learning. 1998. Available from: <http://citeseerx.ist.psu.edu/viewdoc/summary?doi=10.1.1.55.1832>. [cited 2022 Aug 29]
28. Dixon JR, Xu J, Dileep V, Zhan Y, Song F, Le VT, et al. Integrative detection and analysis of structural variation in cancer genomes. *Nat Genet.* 2018;50:1388–98.
29. Kong A, Frigge ML, Masson G, Besenbacher S, Sulem P, Magnusson G, et al. Rate of *de novo* mutations and the importance of father's age to disease risk. *Nature.* 2012;488:471–5.
30. Rahbari R, Wuster A, Lindsay SJ, Hardwick RJ, Alexandrov LB, Turki SA, et al. Timing, rates and spectra of human germline mutation. *Nat Genet.* 2016;48:126–33.
31. Carvalho CMB, Pehlivan D, Ramocki MB, Fang P, Alleva B, Franco LM, et al. Replicative mechanisms for CNV formation are error prone. *Nat Genet.* 2013;45:1319–26.
32. Coulondre C, Miller JH, Farabaugh PJ, Gilbert W. Molecular basis of base substitution hotspots in *Escherichia coli*. *Nature.* 1978;274:775–80.
33. Laskowski RA, Stephenson JD, Sillitoe I, Orengo CA, Thornton JM. VarSite: disease variants and protein structure. *Protein Sci.* 2020;29:111–9.
34. Ferla MP, Pagnamenta AT, Damerell D, Taylor JC, Marsden BD. MichelaN-glo: sculpting protein views on web pages without coding. *Bioinformatics.* 2020;36:3268–70.
35. Riggs ER, Andersen EF, Cherry AM, Kantarci S, Kearney H, Patel A, et al. Technical standards for the interpretation and reporting of constitutional copy-number variants: a joint consensus recommendation of the American College of Medical Genetics and Genomics (ACMG) and the Clinical Genome Resource (ClinGen). *Genet Med.* 2020;22:245–57.
36. Yuan B, Harel T, Gu S, Liu P, Burglen L, Chantot-Bastaraud S, et al. Nonrecurrent 17p11.2p12 rearrangement events that result in two concomitant genomic disorders: the *PMP22-RAI1* contiguous gene duplication syndrome. *Am J Hum Genet.* 2015;97:691–707.
37. Hiratani I, Ryba T, Itoh M, Yokochi T, Schwaiger M, Chang C-W, et al. Global reorganization of replication domains during embryonic stem cell differentiation. *PLoS Biol.* 2008;6:e245.
38. McArthur E, Capra JA. Topologically associating domain boundaries that are stable across diverse cell types are evolutionarily constrained and enriched for heritability. *Am J Hum Genet.* 2021;108:269–83.
39. Pope BD, Ryba T, Dileep V, Yue F, Wu W, Denas O, et al. Topologically associating domains are stable units of replication-timing regulation. *Nature.* 2014;515:402–5.
40. Willis NA, Frock RL, Menghi F, Duffey EE, Panday A, Camacho V, et al. Mechanism of tandem duplication formation in *BRCA1*-mutant cells. *Nature.* 2017;551:590–5.
41. Ju YS, Martincorena I, Gerstung M, Petljak M, Alexandrov LB, Rahbari R, et al. Somatic mutations reveal asymmetric cellular dynamics in the early human embryo. *Nature.* 2017;543:714–8.
42. Johnson A, O'Donnell M. Cellular DNA replicases: components and dynamics at the replication fork. *Annu Rev Biochem.* 2005;74:283–315.
43. Handa T, Kanke M, Takahashi TS, Nakagawa T, Masukata H. DNA polymerization-independent functions of DNA polymerase epsilon in assembly and progression of the replisome in fission yeast. *Mol Biol Cell.* 2012;23:3240–53.
44. Zhou JC, Janska A, Goswami P, Renault L, Abid Ali F, Kotecha A, et al. CMG-Pol epsilon dynamics suggests a mechanism for the establishment of leading-strand synthesis in the eukaryotic replisome. *Proc Natl Acad Sci U S A.* 2017;114:4141–6.
45. Bergstralh DT, Sekelsky J. Interstrand crosslink repair: can XPF-ERCC1 be let off the hook? *Trends Genet.* 2008;24:70–6.
46. Wood RD. Mammalian nucleotide excision repair proteins and interstrand crosslink repair. *Environ Mol Mutagen.* 2010;51:520–6.
47. Niedernhofer LJ, Garinis GA, Raams A, Lalai AS, Robinson AR, Appeldoorn E, et al. A new progeroid syndrome reveals that genotoxic stress suppresses the somatotroph axis. *Nature.* 2006;444:1038–43.
48. Narang A, Uppilli B, Vivekanand A, Naushin S, Yadav A, Singhal K, et al. Frequency spectrum of rare and clinically relevant markers in multiethnic Indian populations (ClinIndb): a resource for genomic medicine in India. *Hum Mutat.* 2020;41:1833–47.
49. Osorio A, Bogliolo M, Fernández V, Barroso A, de la Hoya M, Caldés T, et al. Evaluation of rare variants in the new fanconi anemia gene *ERCC4* (FANCO) as familial breast/ovarian cancer susceptibility alleles. *Hum Mutat.* 2013;34:1615–8.
50. Kumar C, Williams GM, Havens B, Dinicola MK, Surtees JA. Distinct requirements within the Msh3 nucleotide binding pocket for mismatch and double-strand break repair. *J Mol Biol.* 2013;425:1881–98.
51. Reynolds MF, Peterson-Roth EC, Bespalov IA, Johnston T, Gurel VM, Menard HL, et al. Rapid DNA double-strand breaks resulting from processing of Cr-DNA cross-links by both MutS dimers. *Cancer Res.* 2009;69:1071–9.
52. Alexandrov LB, Nik-Zainal S, Wedge DC, Campbell PJ, Stratton MR. Deciphering signatures of mutational processes operative in human cancer. *Cell Rep.* 2013;3:246–59.
53. Kaplanis J, Ide B, Sanghvi R, Neville M, Danecek P, Coorens T, et al. Genetic and chemotherapeutic influences on germline hypermutation. *Nature.* 2022;605:503–8 (Nature Publishing Group).
54. Lupski JR. Structural variation mutagenesis of the human genome: Impact on disease and evolution. *Environ Mol Mutagen.* 2015;56:419–36.
55. Ricard G, Molina J, Chrast J, Gu W, Gheldof N, Pradervand S, et al. Phenotypic consequences of copy number variation: insights from Smith-Magenis and Potocki-Lupski syndrome mouse models. *PLoS Biol.* 2010;8:e1000543.
56. Heck DH, Gu W, Cao Y, Qi S, Lacaria M, Lupski JR. Opposing phenotypes in mice with Smith-Magenis deletion and Potocki-Lupski duplication syndromes suggest gene dosage effects on fluid consumption behavior. *Am J Med Genet A.* 2012;158A:2807–14.
57. Quintero-Rivera F, Eno CC, Sutanto C, Jones KL, Nowaczyk MJM, Wong D, et al. 5q35 duplication presents with psychiatric and undergrowth phenotypes mediated by *NSD1* overexpression and mTOR signaling downregulation. *Hum Genet.* 2021;140:681–90.
58. Coe BP, Witherspoon K, Rosenfeld JA, van Bon BWM, Vulto-van Silfhout AT, Bosco P, et al. Refining analyses of copy number variation identifies specific genes associated with developmental delay. *Nat Genet.* 2014;46:1063–71 (Nature Publishing Group).
59. Firth HV, Richards SM, Bevan AP, Clayton S, Corpas M, Rajan D, et al. DECIPHER: database of chromosomal imbalance and phenotype in humans using Ensembl resources. *Am J Hum Genet.* 2009;84:524–33.
60. Radio FC, Pang K, Cioffi A, Levy MA, Hernández-García A, Pedace L, et al. *SPEN* haploinsufficiency causes a neurodevelopmental disorder overlapping proximal 1p36 deletion syndrome with an epistatue of X chromosomes in females. *Am J Hum Genet.* 2021;108:502–16.
61. Posey JE, Harel T, Liu P, Rosenfeld JA, James RA, CobanAkdemir ZH, et al. Resolution of disease phenotypes resulting from multilocus genomic variation. *N Engl J Med.* 2017;376:21–31 (Massachusetts Medical Society).
62. Du H, Jolly A, Grochowski CM, Carvalho CMB, Liu P. Multiple *de novo* copy number variant (*MdnCNV*) driven mirror traits and blended phenotype. *Gene Expression Omnibus GSE176427*. Available from: <https://www.ncbi.nlm.nih.gov/geo/query/acc.cgi?acc=GSE176427>. [cited 2022 Sep 30]

Publisher's Note

Springer Nature remains neutral with regard to jurisdictional claims in published maps and institutional affiliations.